ACS APPLIED MATERIALS & INTERFACES
Research Article
www.acsami.org

Tuning the Electronic Structure of Tin Sulfides Grown by Atomic Layer Deposition

Giyul Ham,[†] Seokyoon Shin,[†] Joohyun Park,[‡] Hagyoung Choi,[†] Jinseo Kim,[§] Young-Ahn Lee,[§] Hyungtak Seo,*[,§] and Hyeongtag Jeon*[,†]

[†]Department of Materials Science and Engineering, Hanyang University, Seoul, 133-791 Korea

[‡]Department of Nanoscale Semiconductor Engineering, Hanyang University, Seoul, 133-791 Korea

[§]Department of Materials Science and Engineering & Department of Energy Systems Research, Ajou University, Suwon, 443-749 Korea

Supporting Information

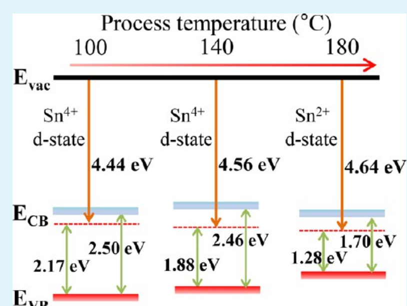

ABSTRACT: In this study, tin sulfide thin films were obtained by atomic layer deposition (ALD) using Tetrakis(dimethylamino)tin (TDMASn, $[(CH_3)_2N]_4Sn$) and hydrogen sulfide (H_2S). The growth rate of the tin sulfides (SnS_x) was shown to be highly dependent on the deposition temperature, and reaction times of 1 second for the TDMASn and H_2S were required to reach the saturation regime. Surface morphologies were smooth or rectangular with rounded corners as observed by a field emission scanning electron microscope (FE-SEM) and were dependent on temperature. X-ray diffraction results confirmed that the crystal structure of SnS_x can be tuned by changing the ALD temperature. Below 120 °C, SnS_x films appeared to be amorphous. In addition, SnS_x films were SnS_2 hexagonal at 140 and 150 °C and SnS orthorhombic above 160 °C. Similarly, the values of the optical band gap and binding energy showed significant differences between 150 and 160 °C. The electronic structures of SnS_x were extracted by UPS and absorption spectroscopy, and the unsaturated Sn 3d molecular orbital (MO) states in the band edge were found to be responsible for the great improvement in electrical conductivity. This study shows that TDMASn-H_2S ALD is an effective deposition method for SnS_x films, offering a simple approach to tune the physical properties.

KEYWORDS: *ALD, TDMASn, SnS_x, tin sulfides, composition, electronic structure*

INTRODUCTION

Among various renewable energy resources including geothermal, tidal, wind, and biomass, solar energy has been the most actively studied because it is infinitely reproducible and possesses no limitations for installation locations. Currently, solar cells based on crystalline silicon show very high conversion efficiencies, but many researchers are studying thin film solar cells since they have lower production costs than crystalline silicon. In particular, copper indium gallium selenide (CIGS) and cadmium telluride (CdTe) solar cells with cadmium sulfide (CdS) buffer layers employing the chemical bath deposition (CBD) method have been widely researched because of their high conversion efficiency.[1] CIGS and CdTe solar cells have many advantages such as high absorption coefficient, direct bandgap, and competitive cost compared to crystalline silicon-based solar cells. Cadmium, however, is a very toxic heavy metal. Also, the CBD method introduces the possibility of contamination because it is not performed in a vacuum. Furthermore, the gallium, indium, and tellurium in CIGS and CdTe cells are rare earth resources that increase process costs.[2] Hence, alternative materials used as absorber or buffer layers should be abundant and nontoxic. Tin sulfides (SnS_x) are alternative candidate materials that circumvent the problems of CIGS and CdTe thin film solar cells with CdS buffer layers because SnS_x materials are relatively less toxic, environmentally friendly, and abundant.

Tin sulfides exist in various composite forms such as SnS, SnS_2, Sn_2S_3, Sn_3S_4, and Sn_4S_5.[3] In practice, the most important compositions of these tin sulfides are SnS and SnS_2. SnS has a twisted sodium chloride structure with germanium sulfide,[4] a p-type property, and an optical band gap of 1.0 to 1.5 eV. SnS_2 has a PbI_2 layered structure with a hexagonal unit cell,[5] an n-type property, and an optical band gap of from 2.2 to 2.4 eV. SnS is a potentially valuable material as an absorber layer in solar cells because it has a high optical absorption coefficient, high quantum yield for the excited carriers, low recombination velocity, and a suitable optical band gap of ~1.3 eV, which is between those of gallium arsenide (1.43 eV) and silicon (1.12 eV).[6] Additionally, SnS is a binary compound, which has a simpler chemistry than multicomponent CIGS.[7] SnS_2 is useful as a buffer layer between the absorber and active layers because it provides effective electron transfer at the interface due to an appropriate energy level distribution.[8] In numerous reports, SnS films have been synthesized by several existing deposition

Received: April 3, 2013
Accepted: August 30, 2013
Published: August 30, 2013

ACS Publications © 2013 American Chemical Society

methods, including chemical bath deposition (CBD),[9,10] RF sputtering,[11] evaporation,[12−15] and electro-deposition.[16] Furthermore, SnS_2 thin films have been deposited by spray pyrolysis,[17] CBD,[18] and chemical vapor deposition (CVD).[19] In this study, we investigated the formation of tin sulfides using atomic layer deposition (ALD) instead of the aforementioned conventional methods.[20−22]

ALD is a method used to deposit thin films based on sequential processing and self-limiting reaction. In comparison to other deposition methods, ALD has several advantages, such as a high thin film quality at relatively low temperatures,[22] precise angstrom (Å)-level control of film thicknesses,[23] high uniformity for large areas, and extremely conformal thin films.[20,21] Deposition of SnS films using ALD was reported by Kim et al. using tin(II) 2,4-pentanedionate $[Sn(acac)_2]$[24] and Sinsermsuksakul et al. using bis(N,N'-diisopropylacetamidinato)tin(II) $[Sn(MeC(N\text{-}^iPr)_2)_2]$[7] as a Sn^{2+} source. These growth rates were 0.24 and 0.90 Å/cycle, respectively. However, to the best of our knowledge, SnS_2 films from ALD have not been reported yet as previous ALD SnS_x films revealed only one type of composition, namely, SnS. Therefore, using the ALD method to achieve a SnS_2 composition is highly desirable and would allow industries to take full advantage of conformal SnS_x films for solar cell applications.

In this work, we report various physical properties of SnS_x thin films grown by thermal ALD using Tetrakis-(dimethylamino)tin (TDMASn, $[(CH_3)_2N]_4Sn$) as a Sn^{4+} source and hydrogen sulfide (H_2S) as a sulfur source for the first time. Furthermore, this ALD process allows one to tune the composition of tin sulfides (SnS and SnS_2) relatively simply by varying the process temperature. The evaluation of the optical band gap, band edge structure, and electrical properties of SnS and SnS_2 suggest a possible application for thin film solar cells.

EXPERIMENTAL SECTION

SnS_x thin films were deposited in a chamber by atomic layer deposition (ALD) using TDMASn and H_2S as the Sn and sulfur sources, respectively. Three types of substrates were prepared for the SnS_x thin film depositions: a thermally oxidized 100 nm SiO_2 layer on a p-type silicon (Si) substrate, a hydrofluoric acid-cleaned p-type Si substrate, and glass (Eagle 2000 glass, Corning Inc.). During the ALD process, a mass flow controller (MFC) controlled the rate of dosing for the Sn precursor and argon (Ar) gas. Ar was used as a bubbler gas at 30 sccm for the TDMASn delivery and as a purging gas at 200 sccm, and the process pressure was maintained at 0.56 Torr. Various pulse times of TDMASn were used, including 0.1, 0.3, 0.5, 1.0, 2.0, and 4.0 seconds (s), at a line temperature of 50 °C with bubbler gas. Likewise, the pulse of H_2S was at a line temperature of 50 °C. The Ar purge time between the TDMASn and H_2S gas pulse was 15 s. Under these operating conditions, one cycle of the optimized ALD at a substrate temperature of 100 °C was defined by the following sequence: TDMASn pulse (1 s)−Ar purge (15 s)−H_2S gas pulse (1 s)−Ar purge (15 s). SnS_x thin films were deposited at various process temperatures using this optimized sequence. The process temperatures ranged from 60 to 180 °C. To verify the I−V trend of these SnS_x films, Pt or Ti electrodes with thicknesses of approximately 50 nm were deposited on the SnS_x films by an e-beam evaporator. The metal electrodes were patterned with a length (L) and width (W) of 1.1 and 0.5 mm, respectively, and the distance between the metal electrodes was 1.2 mm.

The dependence of thickness and surface morphology of the deposited SnS_x thin films on the process temperature was observed using a field emission scanning electron microscope (FE-SEM) and an atomic force microscope (AFM). The crystal structure of 50 nm-thick SnS_x thin films was analyzed by X-ray diffraction (XRD) using Cu Kα radiation (1.54 Å) and a high-resolution transmission electron microscope (HRTEM). Optical properties were measured by ultraviolet−visible spectroscopy at room temperature. Changes in chemical bonding and the elemental composition of SnS_x thin films were analyzed using X-ray photoelectron spectroscopy (XPS) with a Mg Kα X-ray source. The binding energy of each element was calibrated using C−C bonds (284.5 eV) in the C 1s binding state. The band structure was analyzed using ultraviolet photoelectron spectroscopy (UPS), while the electrical properties of the metal/SnS_x were analyzed via an I−V measurement.

RESULTS AND DISCUSSION

The film deposition studies were carried out using TDMASn as a Sn source and H_2S as a sulfur source. Figure 1a and its inset plot show the growth rate of SnS_x films deposited for 500 cycles as a function of TDMASn and the H_2S pulse time using pulse sequences A and B (A: X−15−1−15 s; B: 1−15−Y−15 s) (X: TDMASn pulse time, Y: H_2S pulse time) at 100 °C, respectively. As shown, the growth rate for TDMASn and H_2S pulse time increased considerably with increasing pulse time but showed a significantly saturated region for pulse times greater than 1 s. Therefore, the pulse times for the TDMASn and H_2S were necessarily over 1 s for each ALD cycle to saturate the growth rate. Also, to determine the substrate

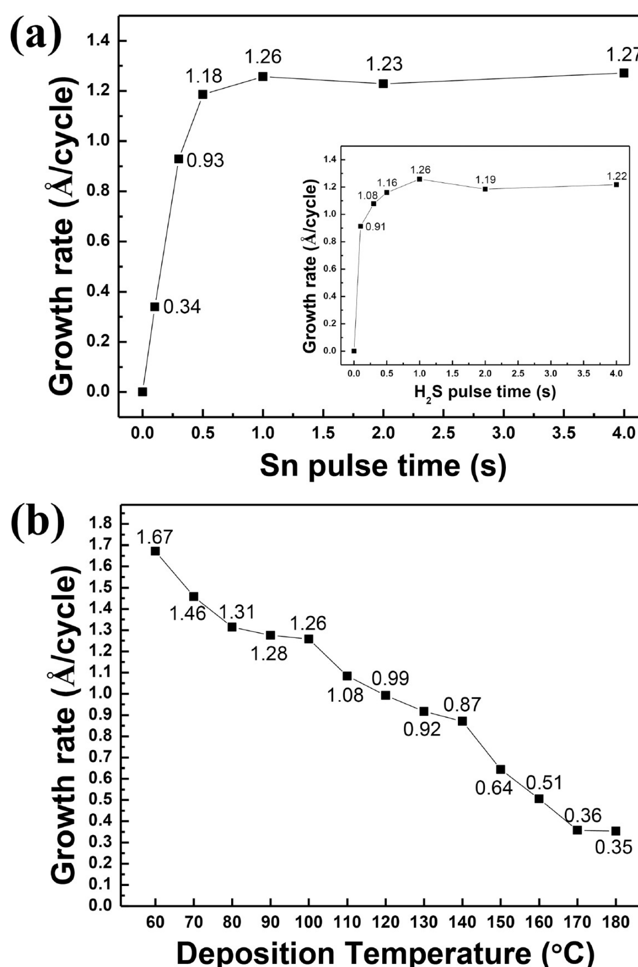

Figure 1. Growth rate (a) for various exposure times of Sn precursor and (b) for 1-second exposure of both the Sn precursor and H_2S as a function of the process temperature. The inset plot is the growth rate for various exposure times of H_2S reactant gas at 100 °C.

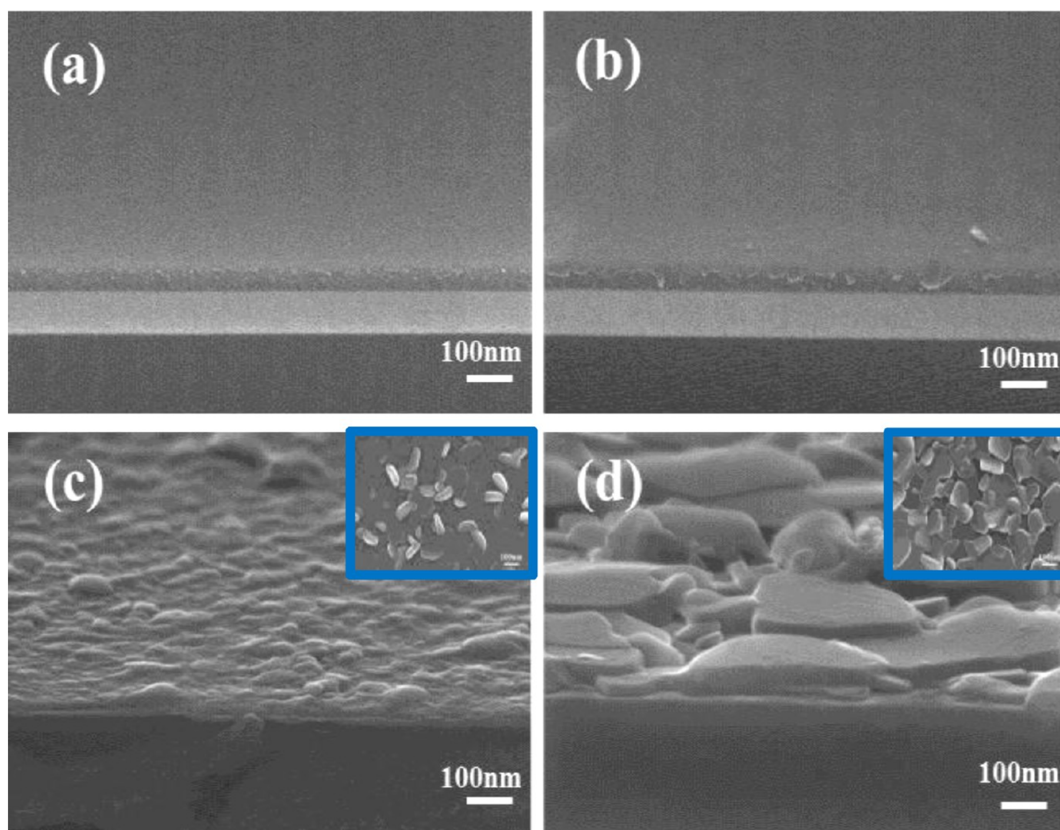

Figure 2. Cross-sectional SEM images of SnS_x films deposited on 100 nm-thick SiO_2 substrates at (a) 120, (b) 140, (c) 160, and (d) 180 °C. Inset image shows the surface morphology.

temperature dependence, SnS_x films were deposited using the optimized pulse sequence (1−15−1−15 s) at temperatures between 60 and 180 °C. As shown in Figure 1b, the growth rate of SnS_x films (after a 500 ALD cycle) generally decreased as the process temperature increased, and then, it decreased rapidly above 140 °C. The growth rate decreased as the deposition temperature was increased. In a previous report, it was noted that the desorption process of reaction species occurred more effectively than the adsorption process of the species on substrates at high temperatures since the supply of more thermal activation energy at higher deposition temperatures resulted in the low growth rate of SnS_x at high deposition temperatures.[23] In addition, SnS_x films were hardly deposited above 200 °C, which was most likely a consequence of the re-evaporation and decomposition of sulfur during the deposition process. The significant variation in the deposition rate of SnS_x films, which depends on the deposition temperature, suggests that the physical and chemical properties differ at various temperatures. Therefore, we investigated the physical and chemical properties of 50 nm-thick SnS_x films deposited at temperatures between 60 and 180 °C using SEM, XRD, XPS, and UV−vis spectroscopy. In order to deposit 50 nm-thick SnS_x films at 60, 80, 100, 120, 140, 150, 160, and 180 °C, we deposited 300, 381, 397, 505, 595, 780, 1389, and 1429 cycles, respectively.

To observe the surface morphology change of SnS_x films as a function of the deposition temperature, SEM analysis was performed. SnS_x films deposited on Si substrate were almost indistinguishable from silicon. The cross-sectional SEM images of several 50 nm-thick SnS_x films deposited on a SiO_2 substrate from 120 to 180 °C are shown in Figure 2. In Figure 2a,b, samples deposited at 120 and 140 °C had smooth surfaces and well-covered SnS_x films. However, samples deposited at 160 and 180 °C revealed rough surfaces with lateral grain expansions, as shown in Figure 2c,d. Upon comparing the samples deposited at 160 °C with those deposited at 180 °C, the grain size of the SnS_x films deposited at 180 °C was considerably larger than those at 160 °C. This discrepancy is due to grain agglomeration, which reduces the surface energy. The dependence of this surface morphological feature on the deposition temperature is similar to the results reported by Sinsermsuksakul et al.[7] From the plan-view SEM images (inner figures), the films above 160 °C had the surface morphology of a square with rounded corners. It was hard to obtain clear plan-view images of deposited films below 140 °C due to the smooth surface. Therefore, SEM analysis indicates that a radical change in surface morphology of ALD SnS_x films occurs depending on the deposition temperature from 120 to 180 °C. In order to clearly analyze the topography of SnS_x films deposited depending on process temperature, we carried out AFM measurements. Figure 3 shows 2-dimensional (2D) images recorded in areas of 2 μm × 2 μm for 50 nm-thick SnS_x films measured by AFM. These images indicate clearly how the topography of the grain surface changes with temperature. As shown in Figure 3a,b, RMS values of SnS_x films at 120 and 140 °C were 0.301 and 0.411 nm, respectively. In other words, the surface of SnS_x films at 120 and 140 °C were very uniform and smooth. Especially above 160 °C, RMS values of SnS films were found to increase from 1.730 to 25.595 nm with increases in deposition temperature. Thus, the size and roughness of the grain surface increased with increasing temperature.

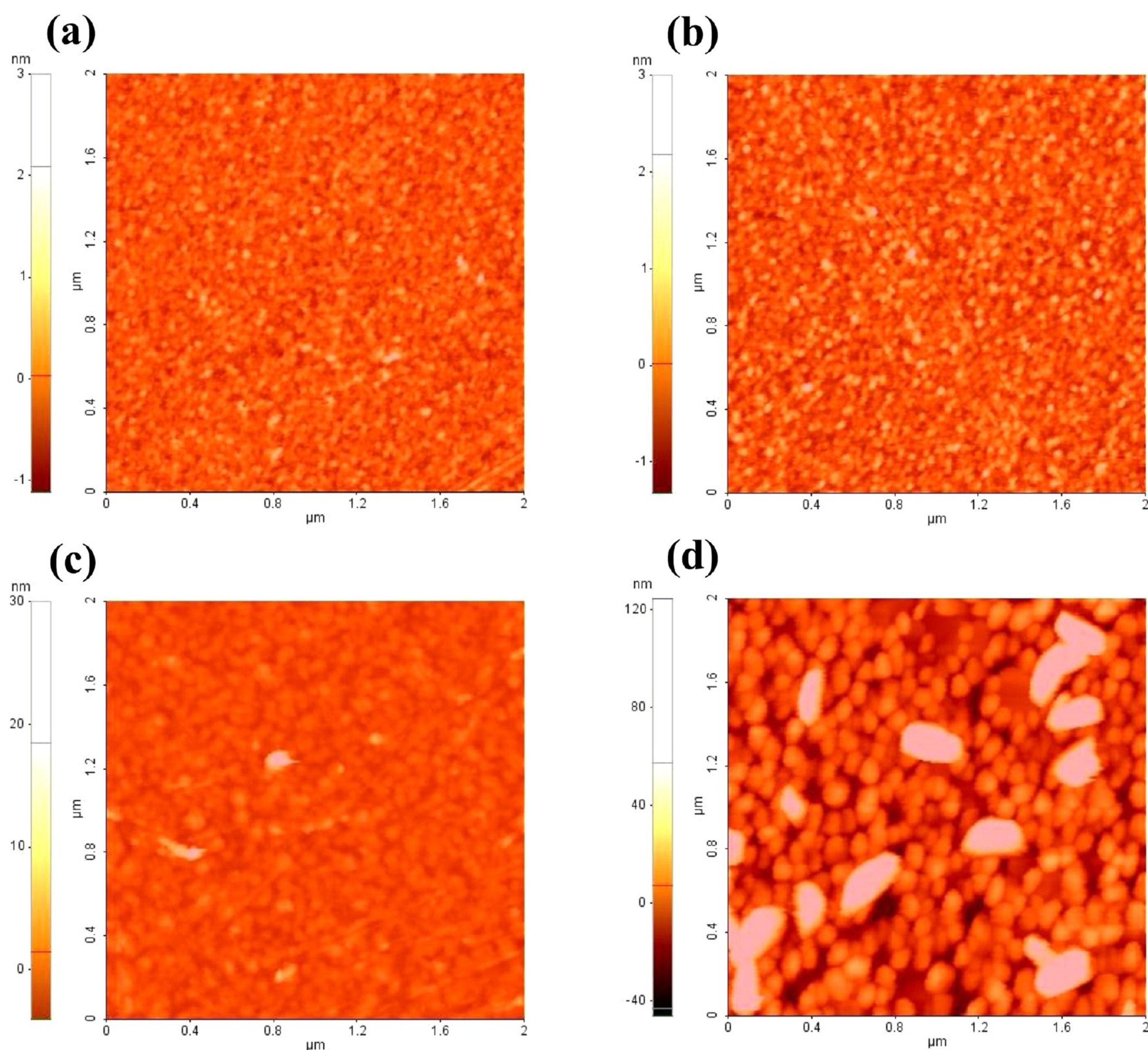

Figure 3. AFM images for 2-dimensional (2D) SnS_x films deposited at (a) 120, (b) 140, (c) 160, and (d) 180 °C.

The XRD spectra of 50 nm-thick SnS_x films deposited from 60 to 180 °C are shown in Figure 4. In the XRD pattern of SnS_x films deposited on Si substrates, a strong peak of diffraction at 33°, corresponding to the silicon (200), was observed in the 2theta/theta mode. Therefore, we investigated the crystal structure of SnS_x films using glancing angle XRD (GAXRD). In the XRD results, the diffraction peaks corresponding to SnS_x films at 60, 80, 100, and 120 °C were not observed. Thus, it was proposed that the crystal structures of the SnS_x films were amorphous below deposition temperatures of 120 °C. On the other hand, the XRD spectra of the SnS_x thin films deposited at 140 and 150 °C showed peaks associated with the (001) SnS_2 hexagonal structure, which were located at 15.02 and 15.04°, respectively (JCPDS No. 23-0677). The multiple diffraction peaks of the SnS_x films deposited at 160 and 180 °C corresponded to the SnS orthorhombic structure, located at 25.7 and 31.6°, corresponding to the (120) and (111) plane, respectively (JCPDS No. 39-0354). Also, the (120) and (111) peak intensities of the SnS_x films deposited at 180 °C were significantly higher than peaks for 160 °C due to the crystallization at the high deposition temperature. Additionally, the SnS_x films deposited at 180 °C showed peaks corresponding to the SnS orthorhombic (131), (141), (002), (151), (122), (231), and (171) peaks as well as the (120) and (111) peaks. These results clearly indicate that the deposition temperature plays an important role in the crystal structure of SnS_x films. In other words, we observed that the SnS_x film crystal structure changed from SnS_2 to SnS and crystallized further with increasing deposition temperatures. Table 1 shows the average grain size calculated from the XRD results by the Scherrer formula,

$$t = 0.9\lambda/(\beta \cos \theta_B) \quad (1)$$

where t denotes the average grain size of the crystal, 0.9 is the constant related to the crystalline shape (Scherrer constant), λ is the wavelength of Cu Kα, β is the full width at half maximum (FWHM) value, and θ_B is the Bragg angle where the peak appears. As shown in Table 1, the crystal size of all the SnS_x

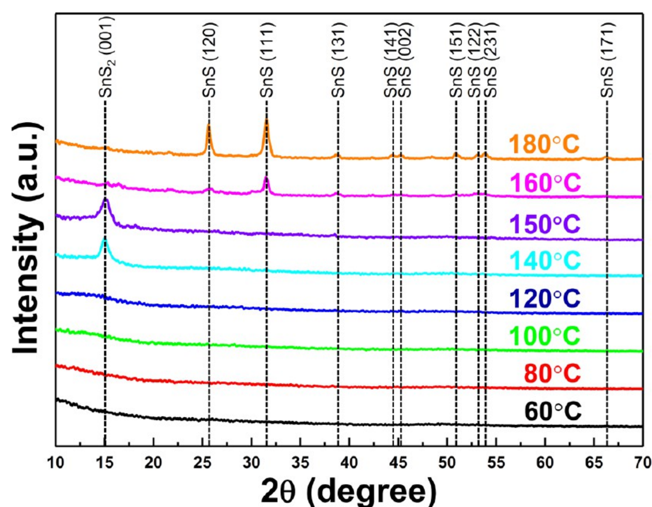

Figure 4. XRD patterns of 50 nm-thick SnS_x films deposited on SiO_2 substrates at different temperatures.

films determined by the Scherrer formula is less than or equal to ~88 Å above 140 °C, and the grain size has a tendency to increase with increasing deposition temperatures. However, the values of grain size calculated by the Scherrer formula are rough estimates because the grain shape is not strictly spherical. The ring-shaped electron diffraction pattern images of SnS_x films taken by TEM analysis are displayed in Figure 5. The samples were prepared by using a precision ion polishing system (PIPS). SnS_x films deposited at 100 °C showed an amorphous structure diffraction pattern, but a polycrystalline ring diffraction pattern was obtained for the SnS_x films deposited above 140 °C. Indexing of the measured ring patterns in Figure 5b,c confirmed that the crystal structures were hexagonal for SnS_2 and orthorhombic for SnS. The ring diffraction patterns of SnS_2 for 140 °C were assigned to be (001), (100), (002), and (110). The diffraction patterns of the SnS films grown at 180 °C were indexed as (101), (201), (111), (311), and (002) of orthorhombic SnS. Therefore, the TEM diffraction pattern results are in accordance with the XRD analysis mentioned above.

The optical properties of SnS_x films were measured on glass substrates in order to investigate the light absorption characteristics for photovoltaic device applications. We have used glass as a substrate which does not affect the analysis results of SnS_x films in the range of 200−1200 nm. Figure 6a shows the measured optical transmittance spectra of the 50 nm-thick SnS_x films deposited from 60 to 180 °C upon the incident monochromatic light with 1 to 6 eV photon energy. As shown in Figure 6a, the average transmittance of films in the visible range of the spectra (from 1.6 to 3.1 eV) gradually decreased from approximately 68.25 to 61.68% by increasing the deposition temperature from 60 to 150 °C. In particular, the transmittance of films deposited above 160 °C changed significantly from those deposited 60 to 150 °C in the visible range. The absorbance spectrum is shown in Figure 6b. Consistent with the transmittance results, absorbance increased with deposition temperature and increased sharply above 160 °C (Figure 6b). We determined the optical band gap using the following relationship

$$(\alpha h\nu)^n = A(h\nu - E_g) \quad (2)$$

From this equation, the direct band gap (E_{dir}) and the indirect band gap (E_{indir}) can be obtained from $n = 2$ and $n = 1/2$, respectively. The inset plot in Figure 6b shows curves of $(\alpha h\nu)^2$ versus $h\nu$ on 50 nm-thick SnS_x films for each temperature. The optical band (E_{dir}) was estimated by determining the intercept of the linear extrapolation with the photon energy for the absorption onset of the $(\alpha h\nu)^2$ curve. Optical band gaps and crystal structures of SnS_x for each temperature are summarized in Table 2. The optical band gap of SnS_x decreased with increasing deposition temperature. Additionally, the optical band gaps of SnS_x largely diminished above 160 °C. The optical band gaps of SnS_x films deposited below 150 °C ranged from 2.47 to 2.76 eV, corresponding to the optical transition between the band edge states of SnS_2. On the other hand, the optical band gaps of from 1.61 to 1.70 eV of SnS_x films deposited above 160 °C were due to the optical transition in the band edge states of SnS. Compared to SnS_2, SnS had additional unsaturated Sn 3d occupied/empty states at the valence/conduction band edge, which led to an optical transition at lower photon energy than band-to-band optical transitions in SnS_2. Consequently, the tunability of the SnS_x crystal structure using the ALD process with varying deposition temperature offers great control over the optical band gap.

In order to obtain data related to elemental compositions, chemical binding states, and valence band edge states of all films, XPS/UPS measurements were performed. SnS_x films exposed to X-rays and ultraviolet light generate photoelectrons. When SnS_x films are analyzed by XPS/UPS, charging effects occur, positively shifting the binding energy of Sn^{2+} and Sn^{4+}. Also, the surface of each film deposited at the various deposition temperatures included carbon and oxygen due to airborne contaminations. After 100 s of Ar sputtering to remove the contamination, oxygen species were not observed in any bulk films, but carbon in the film deposited below 100 °C was still observed (not shown here) because the CH_3 ligand decomposition from the TDMASn precursor did not proceed to completion due to insufficient thermal energy. Figure 7a,b shows the XPS Sn $3d_{5/2}$ and S $2p_{3/2}$ spectra for each SnS_x film deposited at 100, 140, 160, and 180 °C on a Si substrate, the binding energy of which was calibrated by taking the binding energy of the C 1s peak (284.5 eV) as a reference. The binding energies of the Sn $3d_{5/2}$ peak for SnS and SnS_2 are reported to

Table 1. Summaries of the Bragg Angle, FWHM Value, and Grain Size for SnS_x Films Deposited on SiO_2 Substrates at 140, 160, and 180 °C, as Calculated by the Scherrer Formula

		Bragg angle (θ_B)			FWHM value			grain size (nm)		
	SnS_2 hexagonal	(001)			(001)			(001)		
temperature (°C)	SnS orthorhombic		(120)	(111)		(120)	(111)		(120)	(111)
140		7.51			0.1578			8.861		
160			12.87	15.77		0.0141	0.0133		10.057	10.829
180			12.82	15.78		0.0084	0.0099		16.932	14.529

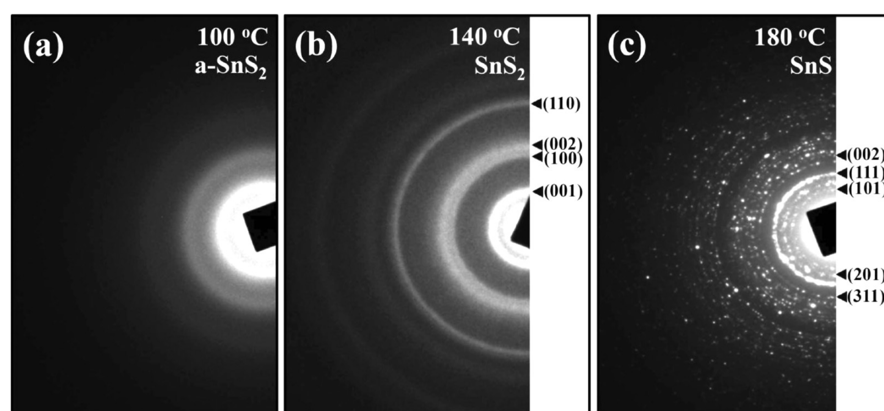

Figure 5. TEM diffraction patterns of 50 nm-thick SnS_x films deposited on Si substrates at 100, 140, and 180 °C.

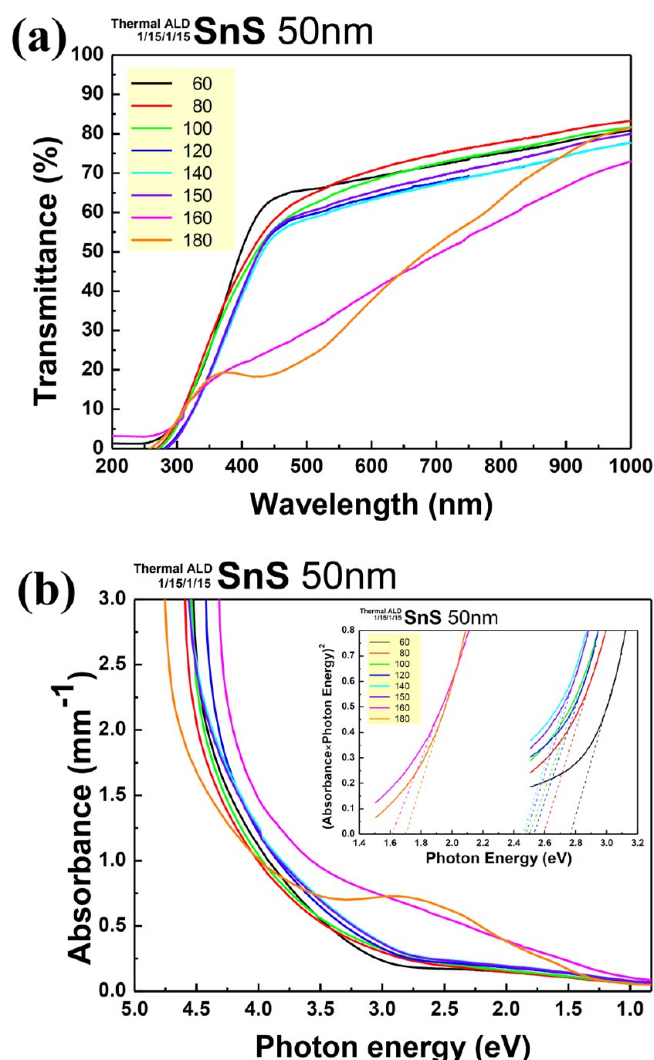

Figure 6. (a) Optical transmission and (b) absorbance curves of SnS_x films deposited on glass substrates at different temperatures. These results were calibrated by taking the transmission and absorbance of the glass substrate as a reference. The inset figure is the direct optical band gap plot estimated from the absorption spectra calculated from $(\alpha h\nu)^2 = A(h\nu - E_g)$.

be 485.7 and 486.6 eV, and the S $2p_{3/2}$ binding energies of SnS and SnS_2 are assigned to 161.0 and 161.6 eV from the literature, respectively.[25] In the XPS spectra, the high binding energies of

Table 2. Summaries of Growth Rate, Crystal Structure, and Optical Band Gap for Each Process Temperature

temperature (°C)	optical bandgap (eV)	crystal structure	growth rate (Å)
60	2.76	amorphous	1.67
80	2.59	amorphous	1.31
100	2.50	amorphous	1.26
120	2.53	amorphous	0.99
140	2.46	SnS_2 hexagonal	0.87
150	2.47	SnS_2 hexagonal	0.64
160	1.61	SnS orthorhombic	0.51
180	1.70	SnS orthorhombic	0.35

Sn $3d_{5/2}$ and S $2p_{3/2}$ corresponding to Sn−S bonding for films deposited below 140 °C were located at 486.6 ± 0.1 and 161.6 ± 0.2 eV. In contrast, SnS_x films above 160 °C had a Sn $3d_{5/2}$ peak of 485.7 ± 0.1 eV and a S $2p_{3/2}$ peak of 161.0 ± 0.1 eV. Thus, the trend of binding energy change in Sn $3d_{5/2}$ and S $2p_{3/2}$ agrees with the stoichiometry conversion from a Sn^{4+} (in SnS_2) dominant phase to a Sn^{2+} (in SnS) dominant phase for increasing deposition temperatures. Figure 7c,d shows UPS spectra for SnS_x samples at the low and high binding energy ranges, respectively. Typically, the binding energy corresponding to the UPS signal onset energy is assigned as the valence band maximum (VBM). However, in the case of SnS_x, such a method for VBM assignment gives the lower-lying VB states, which are considered occupied molecular orbital (MO) states, counterparts of the absorption band at 4 eV in Figure 6b. In contrast, as used in the band gap extraction in the absorption data, the onset energies for the lower UPS signal exist, as shown in the inset of Figure 7c. These onset valence band edge energies were estimated by linear fitting and were reduced from 2.17 to 1.28 eV as the growth temperature increased. This reduction of VBM energy exhibits a trend similar to the optical absorption result. From the UPS and absorption data, the relatively weak, empty, and occupied states of SnS were clearly observed but constitute the valence band and conduction band edges at the lower transition energies, leading to the band gap reduction. Furthermore, since the photoelectron cutoff occurs at a lower kinetic energy than the work function of a given material, we were able to determine the work function using the UPS signal cut off energy at the high binding energy. The work functions of the SnS_x samples were not significantly different, but they were blue-shifted from 4.44 to 4.64 eV as SnS_2 was reduced to SnS.

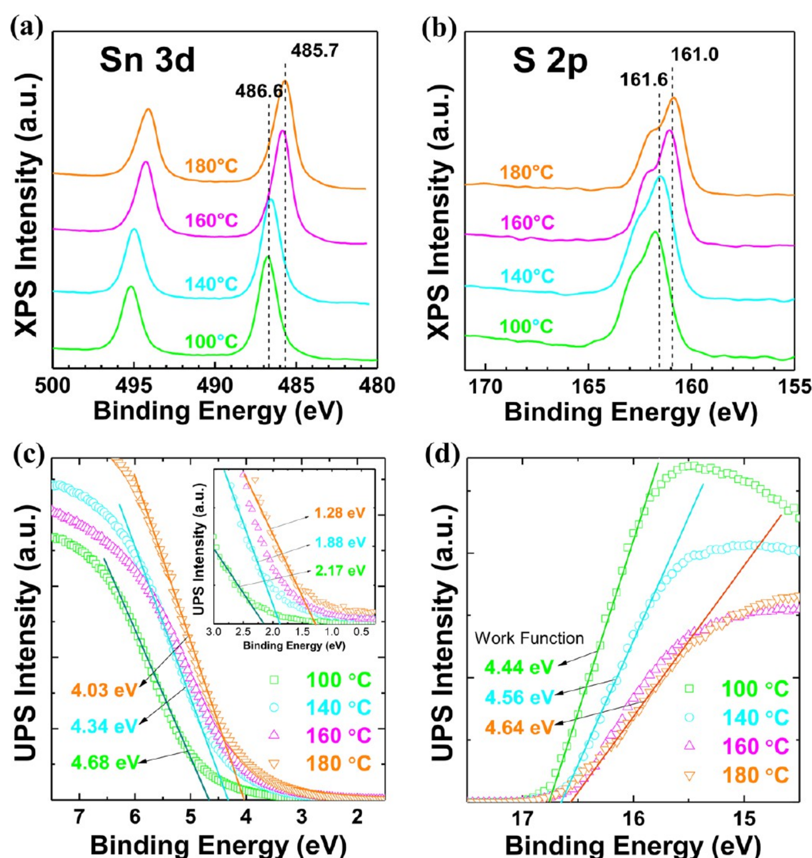

Figure 7. XPS spectra of (a) Sn $3d_{5/2}$ and (b) S $2p_{3/2}$, and UPS spectra of (c) low binding energy range for VBM estimation and (d) high binding energy range for work function calculation for SnS_x films deposited on Si substrates at 100, 140, 160, and 180 °C.

The band electronic structures for amorphous SnS_2, hexagonal SnS_2, and orthorhombic SnS were constructed (Figure 8a) using the optical absorption and UPS analysis since the band gap, work function, and VBM energies were known from those measurements. On the basis of the spectroscopic analysis and as shown in Figure 8a, SnS_2 showed an n-type band electronic structure since the Fermi energy levels (E_F) were closer to the conduction band. The work function in the reduced SnS is larger than SnS_2, indicating the conversion of electronic properties toward a p-type character. Nevertheless, the electronic band structure of SnS is still amphoteric in character rather than strong p-type as reported in previous literature.[7] Previously, it was reported that SnS typically showed p-type character,[7,24] but our SnS film characterized by UPS showed an n-type like character, as shown in Figure 8a. This is due to the surface sensitive probing depth of UPS at >1 nm. In this surface region, oxygen is necessarily distributed in the lattice and the exact chemical state is SnO_xS_y where Sn−O molecular orbital states introduce the partial n-type character in the SnS matrix. This O-related surface state is unavoidable in air and may compromise the interface properties of p-type SnS upon application of heterojunctions. We believe that might be due to the fact that the stoichiometry of SnS_x was subject to significant inhomogeneity depending on the growth techniques and conditions.

For charge transport properties, we fabricated a resistor using Pt, Ti, and Au metal contacts with a contact area of 0.55 mm^2 and a channel length of 1.2 mm to examine the metal/semiconductor contact characteristics. During the *I*−*V* measurement, electron or hole carriers only have to flow through the SnS_x films. Thus, Si substrates coated with thermally deposited 100 nm-thick SiO_2 were used as a substrate. The Ti and Pt contacts for SnS deposited at 180 °C have shown slight rectifications in previous studies, but the current levels were not different from each other. The best ohmic contact to SnS was achieved by the Au contact, exhibiting a clear linear ohmic *I*−*V* behavior. The dependence of this *I*−*V* trend on the type of metal might be related to the work function of each metal. Resistivity values of SnS_x were therefore measured using the resistors with an Au contact. Figure 8b shows resistivity as a function of ALD growth temperature. *I*−*V* characteristics of the SnS_x films deposited below 140 °C were not measured because they were too insulating; their current levels were less than a picoampere. As shown in Figure 8b, the upper limit resistivity of SnS_x without the Au/SnS_x contact resistance correction decreased by two orders of magnitude from $\sim 10^4$ to 10^2 Ω·cm by reducing SnS_2 (deposited at 140 °C) to SnS (deposited at 180 °C). This increase of conductivity in SnS was due to the charge transport at the unsaturated Sn 3d MO states. In the UPS and optical absorption spectra, these states were shown to narrow the band gap of the extended band edge states. Thus, the ALD process of SnS_x developed in this study offers great variability in the electrical conduction of SnS_x through electronic band structure manipulation via thermal chemical composition control.

■ CONCLUSION

In conclusion, we successfully developed an ALD process for SnS_x film deposition for multiple compositions, including SnS and SnS_2. SnS_x films were deposited via ALD onto Si(100), 100

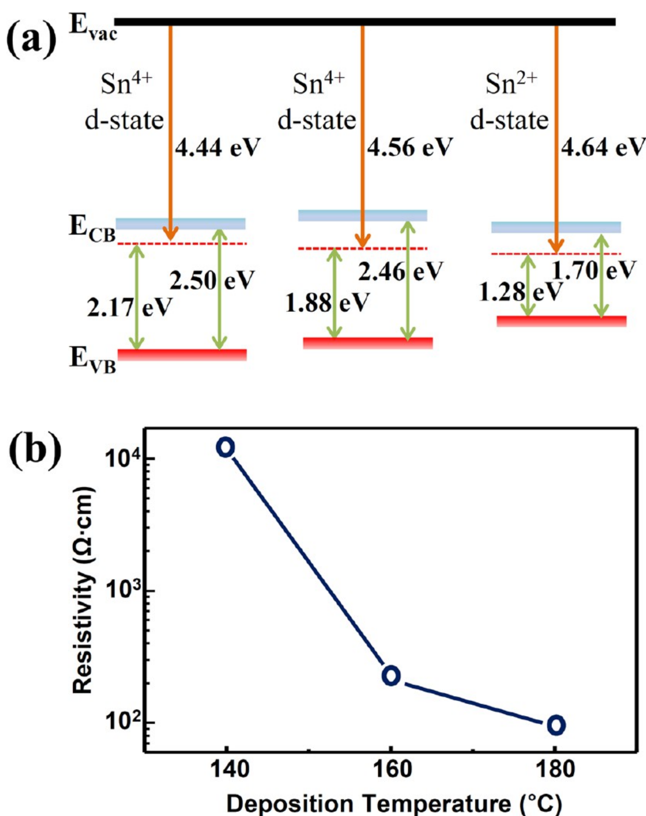

Figure 8. (a) Band electronic structures for SnS_2 at 100 °C (left), SnS_2 at 140 °C (middle), and SnS at 180 °C (right) constructed from the optical absorption and (b) UPS analysis and resistivity of SnS_x extracted from the Au/SnS_x resistor as a function of the growth temperature.

nm-thick SiO_2, and glass substrates using TDMASn as a Sn source and hydrogen sulfide as a sulfur source with deposition temperatures ranging from 60 to 180 °C. To obtain a saturation growth rate, a minimum pulse time of 1 s was required for both TDMASn and H_2S in each ALD cycle. SnS_x films below 120 °C were amorphous and had no diffraction peaks. Moreover, when the deposition temperature increased from 150 to 160 °C, the crystal structure of the films changed from SnS_2 hexagonal to SnS orthorhombic. Similarly, the optical band gaps of the films deposited with increasing temperature decreased from 2.47 eV for the SnS_2 to 1.61 eV for the SnS. XPS results confirmed that SnS_x films deposited below 140 °C and above 160 °C showed Sn $3d_{5/2}$ and S $2p_{3/2}$ states, corresponding to SnS_2 and SnS, respectively. Therefore, it is possible to tune the composition and crystalline features of SnS_x by varying the deposition temperature with a low thermal budget. The electronic structures of SnS_x were extracted by UPS and absorption spectroscopy analysis, and unsaturated Sn 3d MO states in the band edge were found to be responsible for the great improvement in electrical conductivity. With these properties, SnS_x films deposited by ALD using TDMASn and H_2S may be used in the absorber and buffer layers in solar cells as well as in other functional devices.

■ ASSOCIATED CONTENT

Supporting Information

Schematic illustration of 50 nm-thick SnS_x devices for I–V measurements; growth rates for various exposure times of Sn precursor and H_2S reactant gas; absorption spectra of SnS_x films. This material is available free of charge via the Internet at http://pubs.acs.org.

■ AUTHOR INFORMATION

Corresponding Authors

*E-mail: hseo@ajou.ac.kr (H. Seo).

*E-mail: hjeon@hanyang.ac.kr (H. Jeon).

Notes

The authors declare no competing financial interest.

■ ACKNOWLEDGMENTS

This study was supported by a National Research Foundation of Korea (NRF) grant funded by the Korean Government (MEST) (No. 2012-0005474). We appreciate Sanghun Lee's assistance with the SEM measurements.

■ REFERENCES

(1) Wadia, C.; Alivisatos, A. P. *Environ. Sci. Technol.* **2009**, *43*, 2072–2077.
(2) Fthenakis, V. M.; Morris, S. C. *Prog. Photovoltaics* **2012**, *20*, 816–831.
(3) Jiang, T.; Ozin, G. A. *J. Mater. Chem.* **1998**, *8*, 1099–1108.
(4) An, C. H.; Tang, K. B. *J. Cryst. Growth* **2002**, *244*, 333–338.
(5) Deshpande, N. G.; Sagade, A. A. *J. Alloys Compd.* **2007**, *436*, 421–426.
(6) Reddy, K. T. R.; Reddy, N. K. *Sol. Energy Mater. Sol. Cells* **2006**, *90*, 3041–3046.
(7) Sinsermsuksakul, P.; Heo. *J. Adv. Energy Mater.* **2011**, *1*, 1116–1125.
(8) Tan, F.; Qu, S. *Nanoscale Res. Lett.* **2011**, *6*, 298.
(9) Avellaneda, D.; Nair, M. T. S. *J. Electrochem. Soc.* **2008**, *155*, D517–D525.
(10) Turan, E.; Kul, M. *J. Phys. D: Appl. Phys.* **2009**, *42*, 245408.
(11) Hartman, K.; Johnson, J. L. *Thin Solid Films* **2011**, *519*, 7421–7424.
(12) Miles, R. W.; Ogah, O. E. *Thin Solid Films* **2009**, *517*, 4702–4705.
(13) Devika, M.; Reddy, K. T. R. *J. Appl. Phys.* **2006**, *100*, 023518.
(14) Johnson, J. B.; Jones, H. *Semicond. Sci. Technol.* **1999**, *14*, 501–507.
(15) Tanusevski, A.; Poelman, D. *Sol. Energy Mater. Sol. Cells* **2003**, *80*, 297–303.
(16) Ichimura, M.; Takeuchi, K. *Thin Solid Films* **2000**, *361*, 98–101.
(17) Lopez, S.; Ortiz, A. *Semicond. Sci. Technol.* **1994**, *9*, 2130–2133.
(18) Liu, S. A.; Yin, X. M. *Mater. Lett.* **2010**, *64*, 2350–2353.
(19) Manasevit, H. M.; Simpson, W. I. *J. Electrochem. Soc.* **1975**, *122*, 444–450.
(20) George, S. M. *Chem. Rev.* **2010**, *110*, 111–131.
(21) Leskela, M.; Ritala, M. *Thin Solid Films* **2002**, *409*, 138–146.
(22) Lee, S.; Bang, S. *Phys. Status Solidi A* **2010**, *207*, 1845–1849.
(23) Puurunen, R. L. *J. Appl. Phys.* **2005**, *97*, 121301.
(24) Kim, J. Y.; George, S. M. *J. Phys. Chem. C* **2010**, *114*, 17597–17603.
(25) Price, L. S.; Parkin, I. P. *Chem. Mater.* **1999**, *11*, 1792–1799.